Geophysical Research Letters

RESEARCH LETTER
10.1029/2024GL109183

Characterizing South Pole Firn Structure With Fiber Optic Sensing

Yan Yang[1], Zhongwen Zhan[1], Martin Karrenbach[2], Auden Reid-McLaughlin[1], Ettore Biondi[1], Douglas A. Wiens[3], and Richard C. Aster[4]

[1]Seismological Laboratory, California Institute of Technology, Pasadena, CA, USA, [2]Seismics Unusual LLC, Brea, CA, USA, [3]Department of Earth, Environmental, and Planetary Sciences, Washington University in St. Louis, St. Louis, MO, USA, [4]Department of Geosciences, Warner College of Natural Resources, Colorado State University, Fort Collins, CO, USA

Key Points:

- Distributed Acoustic Sensing repurposes an 8 km fiber-optic cable at the South Pole into a dense seismic array
- Gathered data resolve 16 dispersion modes at frequencies up to 100 Hz that constrain P- and S-wave velocities in the firn layer
- Previous density-velocity empirical relations overestimate the dry firn density at South Pole

Supporting Information:

Supporting Information may be found in the online version of this article.

Correspondence to:

Y. Yang,
yanyang@caltech.edu

Citation:

Yang, Y., Zhan, Z., Karrenbach, M., Reid-McLaughlin, A., Biondi, E., Wiens, D. A., & Aster, R. C. (2024). Characterizing South Pole firn structure with fiber optic Sensing. *Geophysical Research Letters*, *51*, e2024GL109183. https://doi.org/10.1029/2024GL109183

Received 8 MAR 2024
Accepted 2 JUL 2024

Abstract The firn layer covers 98% of Antarctica's ice sheets, protecting underlying glacial ice from the external environment. Accurate measurement of firn properties is essential for assessing cryosphere mass balance and climate change impacts. Characterizing firn structure through core sampling is expensive and logistically challenging. Seismic surveys, which translate seismic velocities into firn densities, offer an efficient alternative. This study employs Distributed Acoustic Sensing technology to transform an existing fiber-optic cable near the South Pole into a multichannel, low-maintenance, continuously interrogated seismic array. The data resolve 16 seismic wave propagation modes at frequencies up to 100 Hz that constrain P and S wave velocities as functions of depth. Using co-located geophones for ambient noise interferometry, we resolve very weak radial anisotropy. Leveraging nearby SPICEcore firn density data, we find prior empirical density-velocity relationships underestimate firn air content by over 15%. We present a new empirical relationship for the South Pole region.

Plain Language Summary Firn, the layer of compacted snow merging into glacial ice covering Antarctica, acts as an insulating blanket that mitigates environmental perturbations to the polar ice sheet. Understanding the density and seismic characteristics of the firn layer helps scientists better infer its properties and variation, including factors relevant to glacial stability and sea level change. Firn density is the major uncertainty source for measuring ice sheet mass changes via satellite and airborne sensing. Traditional methods of assessing firn density involve drilling or snow pit analyses and are expensive and time-consuming. We utilize the rapidly developing technology of Distributed Acoustic Sensing to transform a data communication cable near the South Pole into a dense array of seismic sensors, allowing us to noninvasively estimate firn properties by studying seismic waves propagating in the firn to assess its physical properties. Our findings suggest that previous parameterizations overestimate firn density by over 5% and underestimate its air content by over 15% and highlight the value of seismology for advancing glaciological and polar region's climate research.

1. Introduction

The Antarctic Ice Sheet (AIS), Earth's largest surface freshwater reservoir, plays an important role as an indicator of climate change and contributor to sea-level change (Shepherd et al., 2018). Firn is a transitional layer from fresh snow to deeper glacial ice (e.g., Gow, 1969), covers 98% of the AIS (Winther et al., 2001), and critically protects it against environmental perturbations (e.g., MacAyeal, 2018; The Firn Symposium team et al., 2024). In warmer ice sheet systems, such as Greenland or the Antarctic Peninsula, firn provides pore space for heat insulation and surface meltwater retention and refreezes into impermeable ice lenses, thus mitigating mass loss through runoff and moderating sea-level change (Dunmire et al., 2024; Harper et al., 2012; Kuipers Munneke et al., 2015; Medley et al., 2022; Noël et al., 2022). Moreover, the firn layer influences the accurate assessment of key factors relevant to climate change, such as satellite altimetry of surface elevation changes and subsequent calculations of AIS mass variations (Arthern & Wingham, 1998; Noël et al., 2018; van Wessem et al., 2018). Variable mass, density, and thickness of the firn layer, influenced by diverse conditions across Antarctica can introduce significant uncertainty when spatially limited measurements are extrapolated to large regions (Boening et al., 2012; Ligtenberg et al., 2011; van den Broeke, 2008).

In situ observations of firn structure can be obtained from snow depth profiles, which sample the upper few meters for density, temperature, and core stratigraphy (e.g., Herron & Langway, 1980; Järvinen et al., 2013; Ligtenberg

et al., 2011). Limitations of this methodology may include inherent sparsity of drilling or snow pit sites, associated logistical costs, and possible shortfalls in capturing deeper firn layer complexities due to limited sampling depth. Complementing in-situ measurements, non-destructive geophysical methods, such as seismic and radar techniques, can noninvasively characterize firn properties (Abbasi et al., 2010; Arthern et al., 2013; Chaput, Aster, Karplus, & Nakata, 2022; Diez et al., 2016; Hollmann et al., 2021; Jones et al., 2023; Weihaupt, 1963). More recently, distributed acoustic sensing (DAS) using optical fibers has emerged as a tool for glacial seismology applications, offering logistical tractability in challenging environments (Booth et al., 2020; Fichtner et al., 2023; Walter et al., 2020; Zhou et al., 2022). DAS transforms a fiber-optic cable into a dense array of uniaxial strainmeters, providing dense spatial and temporal wavefield resolution across distances up to 100 km (Fan et al., 2023; Lindsey & Martin, 2021; Zhan, 2020). The firn layer's unusual seismic properties, characterized by low near-surface velocities, high degree of lateral homogeneity, and strong near-surface velocity gradient, hosts multiple wave propagation states such as surface wave overtones and leaking modes (Chaput, Aster, Karplus, Nakata, et al., 2022; Kennett, 2023). Utilizing DAS's high-density seismic wavefield sampling, these modes can be characterized and used to refine estimates of firn seismic velocities and structure.

In this work, we leverage an 8 km preexisting buried data communication fiber-optic cable near the South Pole, converting it into a dense seismic array with 1 m spatial sampling. Through active seismic surveys, we resolve the seismic velocity of the firn layer. Additionally, we deployed co-located three-component geophones and conducted seismic ambient noise analysis, allowing us to investigate the radial anisotropy of the firn. Our goal is to advance understanding of the seismic velocity characteristics of firn, specifically applied here to the dry and cold firn layer of the polar plateau region, which is generally characteristic of much of East Antarctica but less extensively investigated than other firn environments.

2. South Pole DAS Experiment and Observations

In January 2023, we utilized a preexisting data fiber-optic cable to create a dense fiber-oriented horizontal strainmeter array with DAS technology. The cable extends between the Amundsen-Scott South Pole Station and the Global Seismographic Network (GSN; Ringler et al., 2022) station QSPA, located at the South Pole Remote Earth Science and Seismological Observatory (SPRESSO) approximately 8 km from the pole (Figure 1; Anthony et al., 2021). The cable, buried about 10 m below the surface, provided a stable temperature and low air circulation environment that facilitated very high signal-to-noise data collection. The fact that the cable is buried 10 m below the surface affects the relative amplitudes of the observed modes but does not affect estimates of phase velocity, nor does it compromise sensitivity to the top 10 m of firn (Figures S1, S2 in Supporting Information S1). An OptaSense QuantX interrogator (Figure 1b), recording at 1,000 Hz sampling rate, produced seismic records from every 1 m along the cable using an 8.2 m gauge (spatial smoothing) length. Along-fiber strain rate data from the DAS system were complemented by twelve co-located Fairfield ZLand three-component geophone nodes spaced about 600 m apart with their transverse components oriented perpendicular to the optical fiber.

Active seismic energy was generated with a propelled energy generator (PEG-40 kg) source. This system is lightweight, highly portable, and engineered for easy mounting onto a Kässbohrer Geländefahrzeug AG PistenBully snow tractor. Repeated impulsive shots were performed for subsequent stacking at two locations aligned with the cable direction, which produced signals with useful frequency content to about 100 Hz. The first set of shots was within the array near its southern terminus (close to DAS Channel 1,000), where we executed 1,066 shots. To mitigate potential bias in firn structure introduced by human vehicle and other activity near the South Pole Station, we executed another 960 shots at a more remote and quiet location beyond the QSPA seismic station, 10 km away from the South Pole station. This latter site experiences minimal human disturbance. The consistency between these two surveys enhances confidence that the seismic conditions described here are indicative of regional conditions in the South Pole and relevant to other regions of interior Antarctica.

We aligned shot onset times and stacked the DAS recorded data (Figure 1c). A 2-D f-k transform was applied to convert these time-space data into the frequency-wavenumber domain. This allowed us to calculate along-fiber phase velocity through dividing the radian frequency by the wavenumber, leading to a detailed frequency-phase velocity (f-v) image that revealed dispersion curves for at least 16 distinct wave propagation modes (Figure 2a). These included Rayleigh wave modes with a cutoff velocity around 2,000 m/s, a leaking mode exceeding 2,000 m/s, and pseudoacoustic modes indicative of surface-reflected P waves trapped in the strong near-surface firn layer seismic velocity gradient (e.g., Albert, 1998) with velocities ranging between 2,000 and 4,000 m/s. The

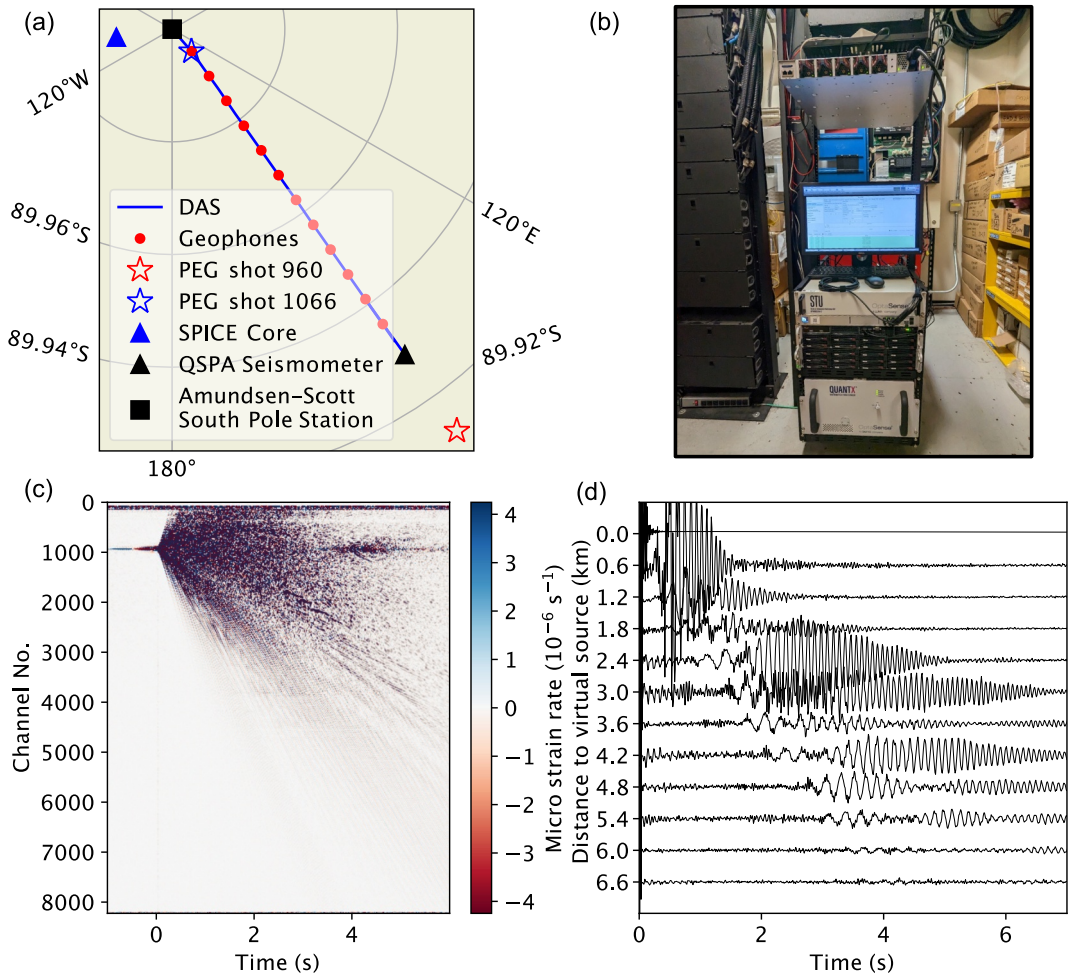

Figure 1. Field setting and observations. (a) The South Pole Quiet Sector, showing the locations of the DAS cable, QSPA site, Ice Core, active shots, and geophone-equipped seismic stations. (b) Interrogator and acquisition monitor installed in the Amundsen-Scott South Pole Station. (c) DAS data, stacked over 1,066 shots applied near Channel 1,000, as shown in (a). (d) Cross correlation functions of transverse geophone components, using the geophone closest to Channel 1,000 as a virtual source.

detailed resolution of multiple firn seismic modes resembles the observations of Fichtner et al. (2023) using airplane landings as a seismic source in Greenland. In our case, the quiet environment at the South Pole (Anthony et al., 2015), a uniformly buried and well-coupled fiber, together with the strong energy stacked from the active surveys allows for still higher signal-to-noise recording and the detection of additional modes.

3. Discrepancies Between Seismic Observations and Velocities Derived From Ice Core Data

Multiple well-resolved seismic wave propagation modes allow us to invert for the vertical seismic firn structure, and to assess these results relative to prior empirical relationships between seismic velocities and density. The South Pole Ice Core (SPICEcore) project, drilled 2.7 km from the Amundsen-Scott South Pole Station in 2014–2016, provided in situ firn density measurements (Winski et al., 2019). The SPICEcore site was selected to ensure proximity to South Pole Station, avoidance of previous station infrastructure and science sectors, and minimal influence from past and present station emissions (Casey et al., 2014). Given its proximity to our study (Figure 1a) and the homogeneous snow and glacial conditions near the South Pole (Watanabe et al., 2003), it provides a reliable firn density data set for this study.

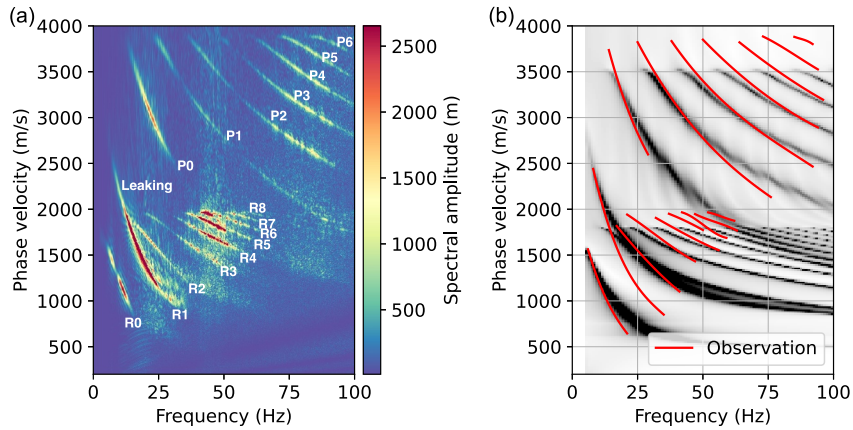

Figure 2. Comparison of observed and synthetic frequency-velocity (*f-v*) Images using prior empirical relations. (a) The *f-v* image computed from the wavefield stacked over 960 active shots that were performed 2 km from the QSPA station (Figure 1a). Identified pseudoacoustic and Rayleigh wave modes are marked in white text. (b) Synthetic *f-v* image derived from SPICEcore (Casey et al., 2014) firn-core density-based seismic velocities using Equations 1 and 2, with red dispersion curves picked from (a).

The work by Kohnen and Bentley (1973) at New Byrd Station provided an early look into seismic velocity-density relationships. The empirical relation between P-wave velocities and density was derived from seismic data and firn density profiles from multiple ice cores (Kohnen, 1972)

$$\rho(z) = \frac{\rho_{ice}}{1 + \left(\frac{V_{P,ice} - V_P(z)}{2250\ \text{m/s}}\right)^{1.22}} \tag{1}$$

where z is depth, $\rho(z)$ is the density in the unit of kg/m^3, $V_P(z)$ is P-wave velocity in units of m/s, and $V_{P,ice}$ is P-wave velocity in the sub-firn ice. The empirical relation between firn density and S-wave velocities was derived on the Alpine glacier Colle Gnifetti (Diez et al., 2014)

$$\rho(z) = \frac{\rho_{ice}}{1 + \left(\frac{V_{S,ice} - V_S(z)}{950\ \text{m/s}}\right)^{1.17}} \tag{2}$$

where $V_S(z)$ is S-wave velocity in the unit of m/s, and $V_{S,ice}$ is S-wave velocity in the sub-firn ice. Using these two equations, we apply $\rho(z)$ from the SPICEcore, $\rho_{ice} = 920$ kg/m^3, $V_{P,ice} = 3{,}810$ m/s, and $V_{S,ice} = 1{,}860$ m/s from a seismic reflection study close to South Pole (Peters et al., 2008) to predict $V_P(z)$ and $V_S(z)$.

Using the empirical $V_P(z)$ and $V_S(z)$ we employed the method of Kennett (2023) to compute the complete seismic response in *f-v* space (Figure 2b) and observed significant discrepancies between observed and predicted wave propagation mode dispersion curves. First, the observed cutoff velocity for the Rayleigh and pseudoacoustic modes is substantially higher than predicted, indicating that sub-firn glacial seismic velocities at the South Pole exceed the values from (1) and (2). Second, discrepancies at high frequencies indicate reduced seismic velocity in the upper firn layers relative to those predicted by (1) and (2).

4. Characterizing Firn Structure With Multimode Seismic Inversion

4.1. Seismic Velocity Model Parameterization

We used the observed multimode dispersion curves to obtain new empirical relation suitable for the firn of the South Pole region. The observational constraints include (normal) Rayleigh modes, leaking modes, and pseudoacoustic modes (Figure 2a). Normal Rayleigh modes are principally sensitive to V_S (e.g., Pan et al., 2019) while leaking modes and pseudoacoustic modes are sensitive to both V_S and V_P (Kennett, 2023; Li et al., 2022; Shi et al., 2022). The prominent presence of multiple leaking and pseudoacoustic modes in our observations thus

enables us to robustly invert for both V_S and V_P. This contrasts with Rayleigh/Love wave surface wave inversions for 1-D models parametrized solely using V_S in which V_P is empirically inferred from V_S due to limited sensitivity. We use a model parameterization with the functional form of (1) and (2) that integrates SPICEcore density data and leverages the relationship between seismic velocities within the dry firn layer and specific coefficients tied to density

$$\rho(z) = \frac{\rho_{ice}}{1 + \left(\frac{V_{x,ice} - V_x(z)}{A_x}\right)^{k_x}} \tag{3}$$

Where x can represent either P or S waves, A_P, A_S are the scaling velocities, and k_P, k_S are exponents determining depth dependence. The upper bounds of the Rayleigh and pseudoacoustic phase velocities approximate $V_{S,ice}$ and $V_{P,ice}$, respectively, enabling us to constrain these values directly from the phase velocity-frequency spectra. This reduces the number of free parameters to four and is applied to fit all observed modes.

4.2. Inversion Framework and Misfit Optimization

Surface wave inversions for seismic structure are most commonly performed by minimizing least-square residuals between fundamental mode groups or phase velocities. Even with advancements incorporating multimode or leaking modes, modal identification can be challenging and is essential prior to applying these methods (e.g., Fichtner et al., 2023; Li et al., 2022). Our method employs an image-based misfit function, which calculates the normalized cross-correlation between two images. We first employ the method introduced by Kennett (2023), to forward model the seismic response in *f-v* space. This circumvents the intricate task of root searching within the complex frequency-wavenumber domain (e.g., Pan et al., 2013) inherent in other methods. Maintaining consistent discretization in velocity and frequency, fitting the synthetic *f-v* image to the observed *f-v* image eliminates the need to individually identify modes. We estimate the unknown parameters in (3) utilizing the ensemble Markov chain Monte Carlo (MCMC) method. We employ the emcee Python package (Foreman-Mackey et al., 2013) for its capability to navigate nonlinear and highly correlated likelihood surfaces typical in forward modeling. The method's convergence is less consistent in expansive model spaces and our streamlined model with only four parameters ensures efficient exploration without excessive computational demands.

Figure 3a illustrates the posterior distributions of our four model parameters from the MCMC simulation. The maximum a posteriori parameters provide a South Pole empirical relation specific to our observations as termed in Equation 3: $A_P = 2{,}283$ m/s,$A_S = 1{,}068$ m/s,$k_P = 1.028$,$k_S = 1.036$, with $V_{P,ice} = 3{,}870$ m/s, and $V_{S,ice} = 1{,}970$ m/s. Figure 3b shows the corresponding maximum a posteriori V_P and V_S model. We present in Figure S3 in Supporting Information S1 the posterior distribution of the inverted V_P and V_S models. The corresponding *f-v* image is shown in Figure 3c overlain with the observed dispersion curves. The close match between model and the high-resolution DAS observation demonstrates the effectiveness of the inversion approach and parameterization using just four free parameters. Results confirm deviations from (1) and (2), with the South Pole region requiring higher seismic velocities in sub-firn ice, larger scaling velocities, and smaller exponents for V_P and V_S.

4.3. Analysis of Radial Anisotropy in South Pole Firn

Inversion with active seismic survey data enables us to resolve the (vertical) radially polarized seismic velocity. Radial anisotropy, in which horizontal elastic parameters differ from those in the vertical direction, has been widely documented in glacial firn (Diez et al., 2016; Pearce et al., 2023; Schlegel et al., 2019; Zhang et al., 2022). Theoretically, Rayleigh waves are sensitive to the vertically polarized V_S (V_{SV}) while Love waves are sensitive to the horizontally polarized V_S (V_{SH}). To investigate potential radial anisotropy, we employ ambient noise interferometry for the transverse geophone components to extract Love wave group velocities. We process 10 days of geophone data following the conventional workflow for ambient noise interferometry (Bensen et al., 2007). The 2–30 Hz cross-correlation data revealed Love wave signals (Figure 1d) for which we conducted a time-frequency analysis to calculate group velocity dispersion (Figure 3d).

Interestingly, the Love wave group velocity was remarkably well fitted using our Rayleigh wave-derived V_{SV} model (Figure 3d), indicating a low degree of radial anisotropy. Studies reporting 10%–15% radial anisotropy ($\frac{V_{SH}}{V_{SV}} - 1$) in the upper 50–60 m of the firn column include Diez et al. (2016) and Pearce et al. (2023). Previous

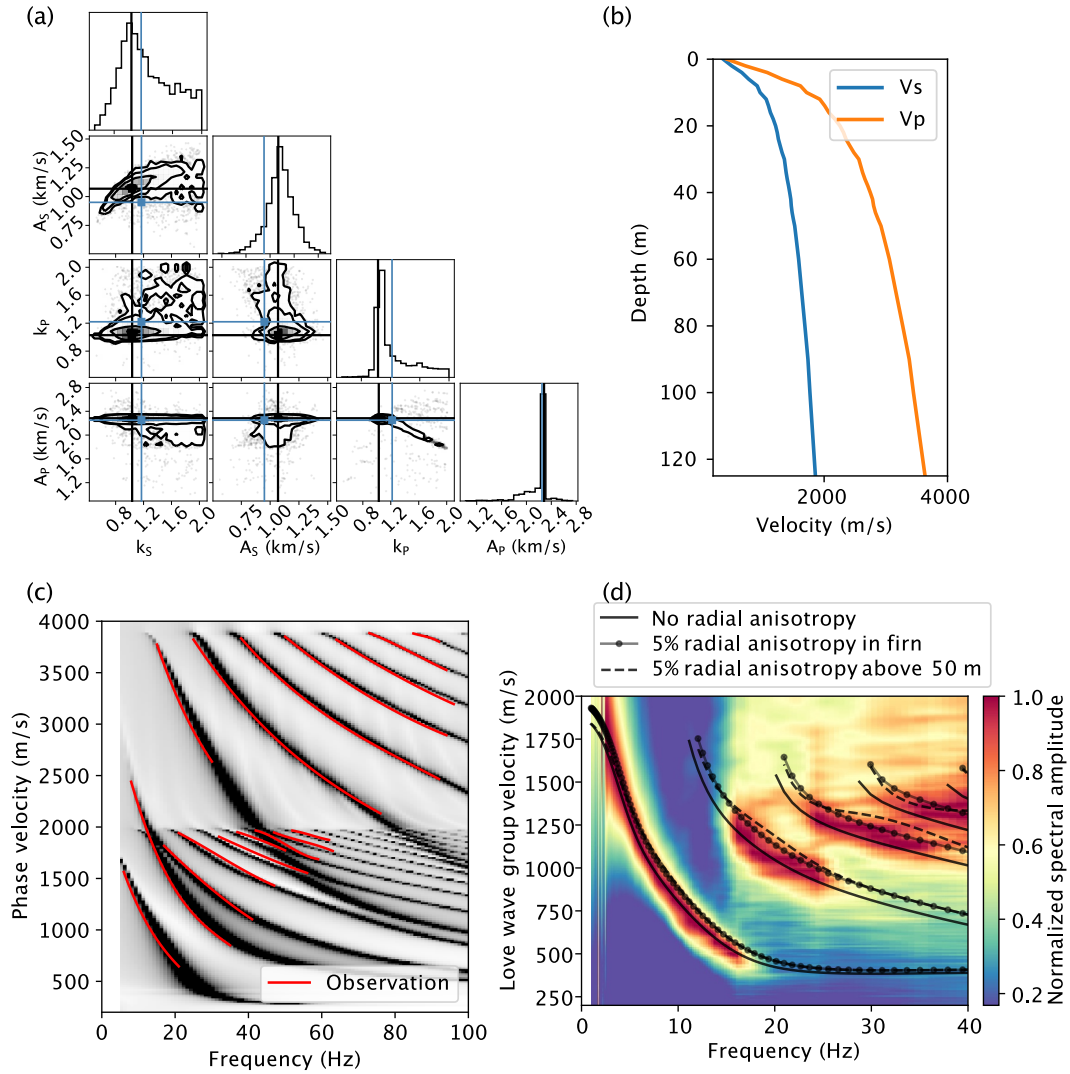

Figure 3. Inverted firn structure and model fitting for the parameters in Equation 3. (a) The posterior distributions of the parameters from our inversion model. The diagonal subplots display marginal distributions as histograms for each parameter and the off-diagonal subplots reveal 2-D marginal distributions between parameter pairs with contours displaying confidence intervals calculated from the sampled posterior distribution. The blue lines within the plot mark the reference values from empirical relations in Equations 1 and 2. The black lines indicate the maximum a posteriori parameters. (b) The maximum a posteriori seismic velocity model. (c) Synthetic *f-v* image using the best-fitting seismic velocity model (b), along with observed dispersion curves in red from Figure 2a. (d) Observed *f-v* image for Love wave group velocities, computed using ambient noise data from fiber co-located geophones (Figure 1d). Solid black synthetic dispersion curves correspond to the (isotropic) model in (b) and dashed and dotted dispersion curves correspond to Love waves with introduced radial anisotropy.

studies typically account for at least 5% radial anisotropy when converting DAS-measured V_{SV} to V_{SH} (Fichtner et al., 2023). In this study, however, adding even 5% radial anisotropy to compute the V_{SH} and the dispersion curves results in a large discrepancy in fitting the Love wave modes, as demonstrated in Figure 3d, confirming that South Pole firn exhibits very weak radial anisotropy.

5. Discussion and Conclusions

5.1. The South Pole Empirical Relation and Its Implication for AIS Mass Change Estimate

Firn density carries information for ice sheet modeling, relevant to meltwater capacity (Medley et al., 2022), solid-ice discharge over the grounding line (Rignot et al., 2019), altimetric mass-balance uncertainty (Smith

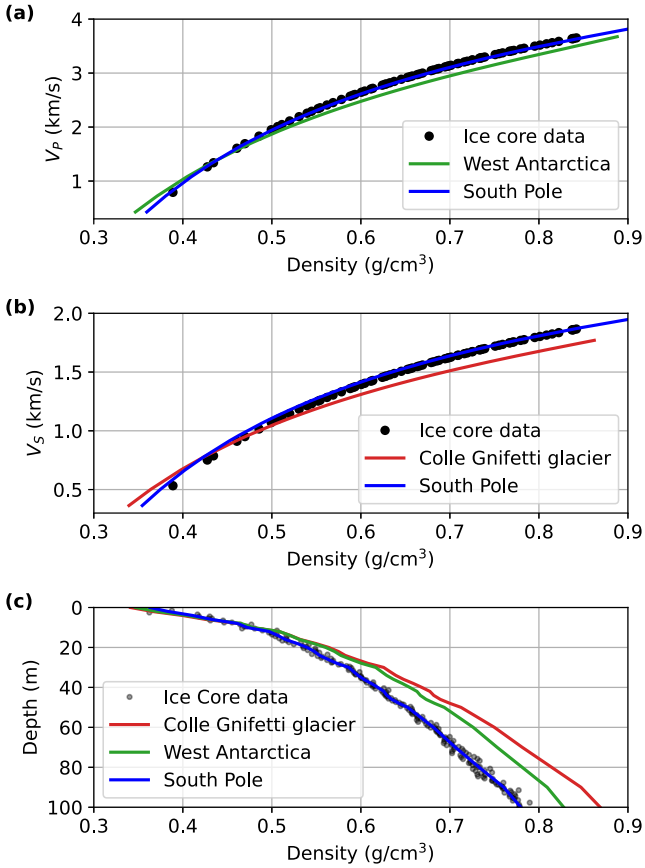

Figure 4. Comparison of empirical relations with the DAS-inverted South Pole seismic velocity model (blue). (a) V_P-density relations; green curve represents empirical relation derived for West Antarctica sites (Equation 1 of Kohnen, 1972); (b) V_S-density relation; red curve represent empirical relation derived for Greenland sites (Equation 2 of Diez et al., 2014); (c) Firn density profiles converted from our seismic velocity model using the three empirical relations. Black dots in all panels indicate data points from the SPICEcore project.

et al., 2023), and paleoclimate reconstruction (Craig et al., 1988). Therefore, it is essential to use validated relationships to translate seismic velocities (V_P or V_S) to the density. Currently, most V_P-density empirical relationships in use have been derived from analyses of multiple boreholes spanning glacial regions worldwide (Kohnen, 1972). In contrast, V_S-density relationships have been specifically derived for the alpine Colle Gnifetti glacier (Diez et al., 2014). These site or region-specific models introduce potential biases when applied to interior Antarctica with contrasting climatic and geophysical characteristics relative to, for example, the warmer, more dynamic environments of interior Greenland and the lower-elevation sectors of West Antarctica. Empirical models based on data from these latter regions underestimate seismic velocity in the dry, cold firn at Kohnen Station in interior Dronning Maud Land (Schlegel et al., 2019) and in this study.

Figures 4a and 4b display relationships between density and V_P, and density and V_S, respectively. Even under the same density (air content), site-specific conditions such as temperature and snow accumulation rates affect the mechanical properties of firn, as evidenced by the difference in seismic velocities. This variation can significantly bias the conversion from seismic velocity to density. In Figure 4c, we plot the depth profiles of density derived from these different empirical relations and juxtapose these against core density observations. The V_P-density relation (1) overestimates density by about 5%, and the V_S-density relation (2) overestimates it by about 8% in the Polar Plateau/East Antarctic context.

From density, we can calculate firn air content (FAC), which is an indicator of the meltwater storage capacity of the firn. Importantly, FAC variability significantly impacts surface height variations observed in satellite altimetry, with over 60% of this variability attributable to FAC changes (Veldhuijsen et al., 2023). FAC can be calculated from firn density and depth (Ligtenberg et al., 2014) as

$$\mathrm{FAC} = \frac{1}{\rho_i} \int_{z_s}^{z(\rho_i)} \left(\rho_i - \rho(z)\right) \mathrm{d}z \tag{4}$$

where $\rho(z)$ is the depth-dependent density, ρ_i is glacial ice density, z_s and $z\,(\rho_i)$ are the surface and the depth at which the ice density is reached, respectively. Calculation using the three different empirical relations (Diez et al., 2014; Kohnen, 1972) suggests that the V_P-density relationship (1) underestimates FAC by about 11%, and the V_S-density model (2) underestimates it by about 17% for East Antarctica. These findings highlight the need for further region-specific empirical relationships that can better capture regional variations necessary for accurate firn density estimations and AIS mass balance estimation.

Results presented here represent a new model for the South Pole, and assessing its broader applicability for interior Antarctica requires additional data collection. Fiber-optic cables are particularly efficient and effective for characterizing seismic wave dispersion and can be readily deployed to acquire more comprehensive data to support or refine these initial findings.

5.2. Weak Radial Anisotropy in South Polar Firn

Firn layer seismic and structural anisotropy, both azimuthal and radial, has been a subject of extensive study. Azimuthal anisotropy, characterized by velocity variations with horizontal direction, is typically observed in firn under the influence of ice flow and surface strain rates, with reported values ranging from 0% to 4% (Chaput et al., 2022a, 2022b; Diez et al., 2016; Hollmann et al., 2021; Zhou et al., 2022). Radial anisotropy, denoting velocity differences between horizontal and vertical polarizations, generally exhibits a larger amplitude. It has been attributed to effective anisotropy from thin layering, intrinsic anisotropy from the preferred orientation of ice

crystals, and to structural anisotropy introduced by features such as aligned crevasses and micro-cracks, which are particularly pronounced in the upper 50 m of the firn layer (Diez et al., 2016; Pearce et al., 2023; Zhang et al., 2022). Observed radial anisotropy is commonly substantial (around 10%–15%).

Our findings near South Pole, a high altitude (2,835 m) plateau characterized by a slowly moving ice sheet (10 m/year), low precipitation (5 cm/year), and cold temperatures (−49.3°C annual average), deviate from observations at other firn locations. We detected negligible radial anisotropy through ambient noise interferometry using the co-located geophones (Figure 3c). A similar observation made at Kohnen Station showed minimal radial anisotropy at depths below 10 m (Schlegel et al., 2019). The absence of radial anisotropy at the South Pole site further underscores the diversity in firn layering characteristics in different Antarctic regions and reiterates the value of localized studies in glacial seismology.

5.3. Potential for Long-Term Fiber-Seismic Monitoring to Glacial Firn Stability and Hydrology

Firn contains significant pore space that can store or transmit meltwater. In the northernmost sectors of Antarctica, the vast majority of surface meltwater is retained and commonly refrozen within the firn, contributing to its stability (Medley et al., 2022), but surface melt is historically scarce to absent in interior Antarctica (Trusel et al., 2012). In Greenland, half of the total surface melt is absorbed by the firn pore spaces (Fettweis et al., 2020). The potential impacts of meltwater on Antarctic mass balance and ice shelf stability—through increased runoff, bed injection, and ice-shelf fracture—underscore the importance of monitoring firn conditions (Bell et al., 2018).

To accurately track the fate of meltwater in the firn system, various observational tools have been employed to monitor near-surface firn properties, ranging from in-situ temperature measurements and dielectric techniques (Miller et al., 2020; Sihvola & Tiuri, 1986), to seismic and radar observations (Chaput et al., 2018; Killingbeck et al., 2020), to remote sensing via synthetic aperture radars and microwave scatterometers (Alley et al., 2018; Fahnestock et al., 1993). The deployment of surface instrumentation on glaciers faces significant challenges due to the harsh and dynamic environment, where seasonal variations in surface morphology due to ablation, crevassing, or melting can compromise data collection or reliability (e.g., MacAyeal, 2018) DAS offers an attractive solution for glacial firn hydrology monitoring (Manos et al., 2024). By utilizing a fiber optic cable, DAS can provide sensitivity in wide areas across multiple glacial features without the typical constraints of traditional seismic sensing methods, such as the need for independent power and other infrastructure at sensing points.

5.4. Conclusions

Distributed Acoustic Sensing (DAS) applied to an 8 km fiber-optic cable near the South Pole and the detection and inversion of 16 seismic propagation modes at frequencies up to 100 Hz enables us to constrain the P- and S-wave velocities of the firn layer. We derive a new empirical relation between density and P- and S-wave velocities for the low precipitation and cold South Pole firn regime that may be applicable to extensive regions of the Antarctic Plateau and interior Antarctica with comparable environmental conditions. This refined model represents an improvement over previous empirical relationships for this site, effectively reducing the underestimation of firn air content by over 15%. This study, more generally, highlights the effectiveness and future potential of fiber-optic sensing technology in glacial seismology.

Acknowledgments
We would like to thank Sheryl Seagraves and Hans Suedhoff of United States Antarctic Program (USAP) for their assistance during the field work. We thank the EarthScope Instrument Center for providing the Propelled Energy Generator for active surveys. We thank Jonathan Kingslake, Benjamin Hills, Zhengbo Li, and Donald Blankenship for insightful discussions. We thank Dr. Emma Pearce and an anonymous reviewer for their constructive suggestions. ZZ was supported by NSF Award 2022920, NSF CAREER Award 1848166, and the Moore Foundation.

Data Availability Statement

The representative active source shots data that are used to generate multimode dispersion and the cross correlation functions that are used to generate Love waves are available online at Yang (2024a). Our final seismic velocity model of South Pole firn is available online at Yang (2024b).

References

Abbasi, R., Abdou, Y., Ackermann, M., Adams, J., Aguilar, J. A., Ahlers, M., et al. (2010). Measurement of sound speed vs. depth in South Pole ice for neutrino astronomy. *Astroparticle Physics*, *33*(5–6), 277–286. https://doi.org/10.1016/j.astropartphys.2010.01.012

Albert, D. G. (1998). Theoretical modeling of seismic noise propagation in firn at the South Pole, Antarctica. *Geophysical Research Letters*, *25*(23), 4257–4260. https://doi.org/10.1029/1998GL900155

Alley, K. E., Scambos, T. A., Miller, J. Z., Long, D. G., & MacFerrin, M. (2018). Quantifying vulnerability of Antarctic ice shelves to hydrofractures using microwave scattering properties. *Remote Sensing of Environment*, *210*, 297–306. https://doi.org/10.1016/j.rse.2018.03.025

Anthony, R. E., Aster, R. C., Wiens, D., Nyblade, A., Anandakrishnan, S., Huerta, A., et al. (2015). The seismic noise environment of Antarctica. *Seismological Research Letters*, *86*(1), 89–100. https://doi.org/10.1785/0220140109

Anthony, R. E., Ringler, A. T., DuVernois, M., Anderson, K. R., & Wilson, D. C. (2021). Six decades of seismology at South Pole, Antarctica: Current limitations and future opportunities to facilitate new geophysical observations. *Seismological Research Letters*, *92*(5), 2718–2735. https://doi.org/10.1785/0220200448

Arthern, R. J., & Wingham, D. J. (1998). The natural fluctuations of firn densification and their effect on the geodetic determination of ice sheet mass balance. *Climatic Change*, *40*(3), 605–624. https://doi.org/10.1023/A:1005320713306

Arthern, R. J. J., Corr, H. F., Gillet-Chaulet, F., Hawley, R. L., & Morris, E. M. (2013). Inversion for the density-depth profile of polar firn using a stepped-frequency radar. *Journal of Geophysical Research: Earth Surface*, *118*(3), 1257–1263. https://doi.org/10.1002/jgrf.20089

Bell, R. E., Banwell, A. F., Trusel, L. D., & Kingslake, J. (2018). Antarctic surface hydrology and impacts on ice-sheet mass balance. *Nature Climate Change*, *8*(12), 1044–1052. https://doi.org/10.1038/s41558-018-0326-3

Bensen, G. D., Ritzwoller, M. H., Barmin, M. P., Levshin, A. L., Lin, F., Moschetti, M. P., et al. (2007). Processing seismic ambient noise data to obtain reliable broad-band surface wave dispersion measurements. *Geophysical Journal International*, *169*(3), 1239–1260. https://doi.org/10.1111/j.1365-246X.2007.03374.x

Boening, C., Lebsock, M., Landerer, F., & Stephens, G. (2012). Snowfall-driven mass change on the East Antarctic ice sheet. *Geophysical Research Letters*, *39*(21). https://doi.org/10.1029/2012GL053316

Booth, A. D., Christoffersen, P., Schoonman, C., Clarke, A., Hubbard, B., Law, R., et al. (2020). Distributed acoustic sensing of seismic properties in a borehole drilled on a fast-flowing Greenlandic outlet glacier. *Geophysical Research Letters*, *47*(13), e2020GL088148. https://doi.org/10.1029/2020GL088148

Casey, K. A., Fudge, T. J., Neumann, T. A., Steig, E. J., Cavitte, M. G. P., & Blankenship, D. D. (2014). The 1500 m South Pole ice core: Recovering a 40 ka environmental record. *Annals of Glaciology*, *55*(68), 137–146. https://doi.org/10.3189/2014AoG68A016

Chaput, J., Aster, R., Karplus, M., & Nakata, N. (2022). Ambient high-frequency seismic surface waves in the firn column of central west Antarctica. *Journal of Glaciology*, *68*(270), 785–798. https://doi.org/10.1017/jog.2021.135

Chaput, J., Aster, R., Karplus, M., Nakata, N., Gerstoft, P., Bromirski, P. D., et al. (2022). Near-surface seismic anisotropy in Antarctic glacial snow and ice revealed by high-frequency ambient noise. *Journal of Glaciology*, *69*(276), 1–17. https://doi.org/10.1017/jog.2022.98

Chaput, J., Aster, R. C., McGrath, D., Baker, M., Anthony, R. E., Gerstoft, P., et al. (2018). Near-surface environmentally forced changes in the ross ice shelf observed with ambient seismic noise. *Geophysical Research Letters*, *45*(20), 11187–11196. https://doi.org/10.1029/2018GL079665

Craig, H., Horibe, Y., & Sowers, T. (1988). Gravitational separation of gases and isotopes in polar ice caps. *Science*, *242*(4886), 1675–1678. https://doi.org/10.1126/science.242.4886.1675

Diez, A., Bromirski, P. D., Gerstoft, P., Stephen, R. A., Anthony, R. E., Aster, R. C., et al. (2016). Ice shelf structure derived from dispersion curve analysis of ambient seismic noise, Ross Ice Shelf, Antarctica. *Geophysical Journal International*, *205*(2), 785–795. https://doi.org/10.1093/gji/ggw036

Diez, A., Eisen, O., Weikusat, I., Eichler, J., Hofstede, C., Bohleber, P., et al. (2014). Influence of ice crystal anisotropy on seismic velocity analysis. *Annals of Glaciology*, *55*(67), 97–106. https://doi.org/10.3189/2014AoG67A002

Dunmire, D., Wever, N., Banwell, A. F., & Lenaerts, J. T. M. (2024). Antarctic-wide ice-shelf firn emulation reveals robust future firn air depletion signal for the Antarctic Peninsula. *Communications Earth & Environment*, *5*(1), 1–13. https://doi.org/10.1038/s43247-024-01255-4

Fahnestock, M., Bindschadler, R., Kwok, R., & Jezek, K. (1993). Greenland ice sheet surface properties and ice dynamics from ERS-1 SAR imagery. *Science*, *262*(5139), 1530–1534. https://doi.org/10.1126/science.262.5139.1530

Fan, C., Li, H., Zhang, K., Liu, H., Sun, Y., Liu, H., et al. (2023). 300 km ultralong fiber optic DAS system based on optimally designed bidirectional EDFA relays. *Photonics Research*, *11*(6), 968–977. https://doi.org/10.1364/PRJ.485701

Fettweis, X., Hofer, S., Krebs-Kanzow, U., Amory, C., Aoki, T., Berends, C. J., et al. (2020). GrSMBMIP: Intercomparison of the modelled 1980–2012 surface mass balance over the Greenland ice sheet. *The Cryosphere*, *14*(11), 3935–3958. https://doi.org/10.5194/tc-14-3935-2020

Fichtner, A., Hofstede, C., N. Kennett, B. L., Nymand, N. F., Lauritzen, M. L., Zigone, D., & Eisen, O. (2023). Fiber-optic airplane seismology on the northeast Greenland ice stream. *The Seismic Record*, *3*(2), 125–133. https://doi.org/10.1785/0320230004

Foreman-Mackey, D., Hogg, D. W., Lang, D., & Goodman, J. (2013). emcee: The MCMC Hammer. *Publications of the Astronomical Society of the Pacific*, *125*(925), 306–312. https://doi.org/10.1086/670067

Gow, A. J. (1969). On the rates of growth of grains and crystals in South polar firn. *Journal of Glaciology*, *8*(53), 241–252. https://doi.org/10.3189/S0022143000031233

Harper, J., Humphrey, N., Pfeffer, W. T., Brown, J., & Fettweis, X. (2012). Greenland ice-sheet contribution to sea-level rise buffered by meltwater storage in firn. *Nature*, *491*(7423), 240–243. https://doi.org/10.1038/nature11566

Herron, M. M., & Langway, C. C. (1980). Firn densification: An empirical model. *Journal of Glaciology*, *25*(93), 373–385. https://doi.org/10.3189/S0022143000015239

Hollmann, H., Treverrow, A., Peters, L. E., Reading, A. M., & Kulessa, B. (2021). Seismic observations of a complex firn structure across the amery ice shelf, East Antarctica. *Journal of Glaciology*, *67*(265), 777–787. https://doi.org/10.1017/jog.2021.21

Järvinen, O., Leppäranta, M., & Vehviläinen, J. (2013). One-year records from automatic snow stations in western Dronning Maud Land, Antarctica. *Antarctic Science*, *25*(5), 711–728. https://doi.org/10.1017/S0954102013000187

Jones, G. A., Ferreira, A. M. G., Kulessa, B., Schimmel, M., Berbellini, A., & Morelli, A. (2023). Constraints on the cryohydrological warming of firn and ice in Greenland from Rayleigh wave ellipticity data. *Geophysical Research Letters*, *50*(15), e2023GL103673. https://doi.org/10.1029/2023GL103673

Kennett, B. (2023). Interacting seismic waveguides: Multimode surface waves and leaking modes. *Seismica*, *2*(1). https://doi.org/10.26443/seismica.v2i1.282

Killingbeck, S. F., Schmerr, N. C., Montgomery, L. N., Booth, A. D., Livermore, P. W., Guandique, J., et al. (2020). Integrated borehole, radar, and seismic velocity analysis reveals dynamic spatial variations within a firn aquifer in southeast Greenland. *Geophysical Research Letters*, *47*(18), e2020GL089335. https://doi.org/10.1029/2020GL089335

Kohnen, H. (1972). Über die Beziehung zwischen seismischen Geschwindigkeiten und der Dichte in Firn und Eis (On the Relation between Seismic Velocities and Density in Firn and Ice). *Geophysik*, *38*(5), 925–935.

Kohnen, H., & Bentley, C. R. (1973). Seismic refraction and reflection measurements at "Byrd" station, Antarctica. *Journal of Glaciology*, *12*(64), 101–111. https://doi.org/10.3189/S0022143000022747

Kuipers Munneke, P., Ligtenberg, S. R. M., Noël, B. P. Y., Howat, I. M., Box, J. E., Mosley-Thompson, E., et al. (2015). Elevation change of the Greenland Ice Sheet due to surface mass balance and firn processes, 1960–2014. *The Cryosphere*, *9*(6), 2009–2025. https://doi.org/10.5194/tc-9-2009-2015

Li, Z., Shi, C., Ren, H., & Chen, X. (2022). Multiple leaking mode dispersion observations and applications from ambient noise cross-correlation in Oklahoma. *Geophysical Research Letters*, *49*(1), e2021GL096032. https://doi.org/10.1029/2021GL096032
Ligtenberg, S. R. M., Helsen, M. M., & van den Broeke, M. R. (2011). An improved semi-empirical model for the densification of Antarctic firn. *The Cryosphere*, *5*(4), 809–819. https://doi.org/10.5194/tc-5-809-2011
Ligtenberg, S. R. M., Kuipers Munneke, P., & van den Broeke, M. R. (2014). Present and future variations in Antarctic firn air content. *The Cryosphere*, *8*(5), 1711–1723. https://doi.org/10.5194/tc-8-1711-2014
Lindsey, N. J., & Martin, E. R. (2021). Fiber-optic seismology. *Annual Review of Earth and Planetary Sciences*, *49*(1), 309–336. https://doi.org/10.1146/annurev-earth-072420-065213
MacAyeal, D. R. (2018). Seismology gets under the skin of the Antarctic ice sheet. *Geophysical Research Letters*, *45*(20), 11173–11176. https://doi.org/10.1029/2018GL080366
Manos, J.-M., Gräff, D., Martin, E., Paitz, P., Walter, F., Fichtner, A., & Lipovsky, B. P. (2024). DAS to discharge: Using distributed acoustic sensing (DAS) to infer glacier runoff. Retrieved from https://eartharxiv.org/repository/view/6680/
Medley, B., Neumann, T. A., Zwally, H. J., Smith, B. E., & Stevens, C. M. (2022). Simulations of firn processes over the Greenland and antarctic ice sheets: 1980–2021. *The Cryosphere*, *16*(10), 3971–4011. https://doi.org/10.5194/tc-16-3971-2022
Miller, O., Solomon, D. K., Miège, C., Koenig, L., Forster, R., Schmerr, N., et al. (2020). Hydrology of a perennial firn aquifer in southeast Greenland: An overview driven by field data. *Water Resources Research*, *56*(8), e2019WR026348. https://doi.org/10.1029/2019WR026348
Noël, B., Lenaerts, J. T. M., Lipscomb, W. H., Thayer-Calder, K., & van den Broeke, M. R. (2022). Peak refreezing in the Greenland firn layer under future warming scenarios. *Nature Communications*, *13*(1), 6870. https://doi.org/10.1038/s41467-022-34524-x
Noël, B., van de Berg, W. J., van Wessem, J. M., van Meijgaard, E., van As, D., Lenaerts, J. T. M., et al. (2018). Modelling the climate and surface mass balance of polar ice sheets using RACMO2 – Part 1: Greenland (1958–2016). *The Cryosphere*, *12*(3), 811–831. https://doi.org/10.5194/tc-12-811-2018
Pan, L., Chen, X., Wang, J., Yang, Z., & Zhang, D. (2019). Sensitivity analysis of dispersion curves of Rayleigh waves with fundamental and higher modes. *Geophysical Journal International*, *216*(2), 1276–1303. https://doi.org/10.1093/gji/ggy479
Pan, Y., Xia, J., & Zeng, C. (2013). Verification of correctness of using real part of complex root as Rayleigh-wave phase velocity with synthetic data. *Journal of Applied Geophysics*, *88*, 94–100. https://doi.org/10.1016/j.jappgeo.2012.09.012
Pearce, E., Zigone, D., Hofstede, C., Fichtner, A., Rimpot, J., Olander Rasmussen, S., et al. (2023). *Firn seismic Anisotropy in the north East Greenland ice Stream from ambient noise surface waves* (preprint). *Ice sheets/Greenland*. https://doi.org/10.5194/egusphere-2023-2192
Peters, L. E., Anandakrishnan, S., Holland, C. W., Horgan, H. J., Blankenship, D. D., & Voigt, D. E. (2008). Seismic detection of a subglacial lake near the South Pole, Antarctica. *Geophysical Research Letters*, *35*(23). https://doi.org/10.1029/2008GL035704
Rignot, E., Mouginot, J., Scheuchl, B., van den Broeke, M., van Wessem, M. J., & Morlighem, M. (2019). Four decades of antarctic ice sheet mass balance from 1979–2017. *Proceedings of the National Academy of Sciences*, *116*(4), 1095–1103. https://doi.org/10.1073/pnas.1812883116
Ringler, A. T., Anthony, R. E., Aster, R. C., Ammon, C. J., Arrowsmith, S., Benz, H., et al. (2022). Achievements and prospects of global broadband seismographic networks after 30 Years of continuous geophysical observations. *Reviews of Geophysics*, *60*(3), e2021RG000749. https://doi.org/10.1029/2021RG000749
Schlegel, R., Diez, A., Löwe, H., Mayer, C., Lambrecht, A., Freitag, J., et al. (2019). Comparison of elastic moduli from seismic diving-wave and ice-core microstructure analysis in Antarctic polar firn. *Annals of Glaciology*, *60*(79), 220–230. https://doi.org/10.1017/aog.2019.10
Shepherd, A., Ivins, E., Rignot, E., Smith, B., van den Broeke, M., Velicogna, I., et al. (2018). Mass balance of the antarctic ice sheet from 1992 to 2017. *Nature*, *558*(7709), 219–222. https://doi.org/10.1038/s41586-018-0179-y
Shi, C., Ren, H., Li, Z., & Chen, X. (2022). Calculation of normal and leaky modes for horizontal stratified models based on a semi-analytical spectral element method. *Geophysical Journal International*, *230*(3), 1928–1947. https://doi.org/10.1093/gji/ggac163
Sihvola, A., & Tiuri, M. (1986). Snow fork for field determination of the density and wetness profiles of a snow pack. *IEEE Transactions on Geoscience and Remote Sensing, GE-*, *24*(5), 717–721. https://doi.org/10.1109/TGRS.1986.289619
Smith, B. E., Medley, B., Fettweis, X., Sutterley, T., Alexander, P., Porter, D., & Tedesco, M. (2023). Evaluating Greenland surface-mass-balance and firn-densification data using ICESat-2 altimetry. *The Cryosphere*, *17*(2), 789–808. https://doi.org/10.5194/tc-17-789-2023
Trusel, L. D., Frey, K. E., & Das, S. B. (2012). Antarctic surface melting dynamics: Enhanced perspectives from radar scatterometer data. *Journal of Geophysical Research*, *117*(F2). https://doi.org/10.1029/2011JF002126
van den Broeke, M. (2008). Depth and density of the antarctic firn layer. *Arctic Antarctic and Alpine Research*, *40*(2), 432–438. https://doi.org/10.1657/1523-0430(07-021)[BROEKE]2.0.CO;2
van Wessem, J. M., van de Berg, W. J., Noël, B. P. Y., van Meijgaard, E., Amory, C., Birnbaum, G., et al. (2018). Modelling the climate and surface mass balance of polar ice sheets using RACMO2 – Part 2: Antarctica (1979–2016). *The Cryosphere*, *12*(4), 1479–1498. https://doi.org/10.5194/tc-12-1479-2018
Veldhuijsen, S. B. M., van de Berg, W. J., Brils, M., Kuipers Munneke, P., & van den Broeke, M. R. (2023). Characteristics of the 1979–2020 Antarctic firn layer simulated with IMAU-FDM v1.2A. *The Cryosphere*, *17*(4), 1675–1696. https://doi.org/10.5194/tc-17-1675-2023
Walter, F., Gräff, D., Lindner, F., Paitz, P., Köpfli, M., Chmiel, M., & Fichtner, A. (2020). Distributed acoustic sensing of microseismic sources and wave propagation in glaciated terrain. *Nature Communications*, *11*(1), 2436. https://doi.org/10.1038/s41467-020-15824-6
Watanabe, O., Jouzel, J., Johnsen, S., Parrenin, F., Shoji, H., & Yoshida, N. (2003). Homogeneous climate variability across East Antarctica over the past three glacial cycles. *Nature*, *422*(6931), 509–512. https://doi.org/10.1038/nature01525
Weihaupt, J. G. (1963). Seismic and gravity studies at the South Pole. *Geophysics*, *28*(4), 582–592. https://doi.org/10.1190/1.1439232
Winski, D. A., Fudge, T. J., Ferris, D. G., Osterberg, E. C., Fegyveresi, J. M., Cole-Dai, J., et al. (2019). The SP19 chronology for the South Pole ice core – Part 1: Volcanic matching and annual layer counting. *Climate of the Past*, *15*(5), 1793–1808. https://doi.org/10.5194/cp-15-1793-2019
Winther, J.-G., Jespersen, M. N., & Liston, G. E. (2001). Blue-ice areas in Antarctica derived from NOAA AVHRR satellite data. *Journal of Glaciology*, *47*(157), 325–334. https://doi.org/10.3189/172756501781832386
Yang, Y. (2024a). Representative data of the South Pole DAS array for firn structure characterization. [Dataset]. https://doi.org/10.22002/424df-j9d14. *CaltechDATA*
Yang, Y. (2024b). Seismic velocity model of South Pole firn. [Dataset]. https://doi.org/10.22002/vqmc4-cea73. *CaltechDATA*
Zhan, Z. (2020). Distributed acoustic sensing turns fiber-optic cables into sensitive seismic antennas. *Seismological Research Letters*, *91*(1), 1–15. https://doi.org/10.1785/0220190112
Zhang, Z., Nakata, N., Karplus, M., Kaip, G., & Yi, J. (2022). Shallow ice-sheet composite structure revealed by seismic imaging near the west antarctic ice sheet (WAIS) divide camp. *Journal of Geophysical Research: Earth Surface*, *127*(12), e2022JF006777. https://doi.org/10.1029/2022JF006777
Zhou, W., Butcher, A., Brisbourne, A. M., Kufner, S.-K., Kendall, J.-M., & Stork, A. L. (2022). Seismic noise interferometry and distributed acoustic sensing (DAS): Inverting for the firn layer S-velocity structure on rutford ice stream, Antarctica. *Journal of Geophysical Research: Earth Surface*, *127*(12), e2022JF006917. https://doi.org/10.1029/2022JF006917